Monthly Notices
of the
ROYAL ASTRONOMICAL SOCIETY

Mon. Not. R. Astron. Soc. **422,** 719–730 (2012) doi:10.1111/j.1365-2966.2012.20651.x

The cluster of galaxies LCDCS-S001 – II. r' and i' photometry, morphological analysis and improved kinematic parameters

S. B. Rembold[1]★ and M. G. Pastoriza[2]

[1]*LATO-DCET-UESC, Rodovia Ilhéus-Itabuna km 16, CEP 45662-000, Ilhéus, Bahia, Brazil*
[2]*IF-UFRGS, Av. Bento Gonçalves 9500, CEP 91350-050, Porto Alegre, Rio Grande do Sul, Brazil*

Accepted 2012 January 30. Received 2012 January 27; in original form 2011 December 31

ABSTRACT

We present photometric parameters of the galaxies in the direction of the galaxy cluster LCDCS-S001 and improved kinematic parameters from new spectroscopic observations. From GMOS multi-object spectroscopy, we have been able to confirm a new set of 10 cluster members, resulting in a total 22 objects from previous observations. With these data, a dispersion velocity of $\sigma = 887 \pm 249\,\mathrm{km\,s^{-1}}$, a virial radius $R_{200} = 0.98 \pm 0.22$ Mpc and a mass of $M_{200} = (5.4 \pm 2.8) \times 10^{14}\,\mathrm{M_\odot}$ have been derived. From GMOS i' and r' images, we have extracted the individual sources and derived their magnitudes, relative positions and the bulge+disc brightness profile decomposition. We show that the cluster has an elongated morphology along the north–south direction, with ellipticity $\varepsilon = 0.49 \pm 0.14$, well represented by a King model with a core radius $R_\mathrm{C} = 283 \pm 66$ kpc, above the typical core radii of regular clusters. It shows at least one local overdensity, north-west from the cluster centre, very compact and with a very high central density. The i' luminosity function of LCDCS-S001 has an almost flat faint-end, $\alpha = -1.16 \pm 0.18$. As for the constituent galaxies, we have found that *a large fraction* of the cluster galaxies are late-type systems. Extensive simulations were made in order to verify the validity of our conclusions. We discuss the implication of these results for the evolutionary status of LCDCS-S001 and conclude that this cluster is still dynamically young.

Key words: galaxies: clusters: general – galaxies: clusters: individual: LCDCS-S001 – galaxies: high-redshift.

1 INTRODUCTION

Galaxy clusters have been extensively studied in recent years due to their special role both in relation to the large-scale mass distribution in the Universe and in the formation and evolution of galaxies themselves (Demarco et al. 2007; Moran et al. 2007). Galaxies with distinct Hubble types are typical of diverse regions, and galaxy clusters offer a dense environment where evolutionary processes, driven by strong interactions with the outside, are accelerated (Kodama et al. 2001; Lewis et al. 2002; Finn et al. 2005). Moreover, galaxy clusters are the largest gravitationally bound structures which have had time to (at least marginally) reach dynamical equilibrium in the Universe. The large-scale distribution of galaxies in the vicinity of clusters comprises filaments and walls, through which accretion of lower mass systems may take place (Tanaka et al. 2005, and references therein). This makes galaxy clusters unique systems to study the processes that drive large-scale mass collapse (and therefore generate constrains on the primordial density fluctuations), and the non-linear, small-scale processes that drive both the interactions between individual darkmatter haloes and the galaxy formation and evolution.

As a result of the accretion and merging processes that feed cluster mass growth, populational, dynamical and structural signatures are expected to be imprinted in both the cluster observables and the properties of its individual galaxies (Hwang & Lee 2009). In particular, massive mergers and accretion of groups of galaxies in infalling dark matter haloes are expected to generate deviations in the original spherical symmetry of a virialized cluster and produce substructures, which can be seen in the projected distribution of galaxies and the radial velocity/velocity dispersion space (Burgett et al. 2004; Boschin, Barrena & Girardi 2009; Bravo-Alfaro et al. 2009). In particular, the projected distribution of ellipticities shows that clusters of galaxies are intrinsically more flat than elliptical galaxies in general (Carter & Metcalfe 1980), and the amount of flattening of the distribution reflects the dynamical stage of the cluster: fully virialized systems are in general more spherical, except in the presence of secondary infall (Plionis 2002). While massive

★E-mail: sbrembold@uesc.br

mergers can dominate the mass growth of galaxy clusters, as seen in *N*-body simulations, accretion of loose associations of low-mass galaxies has been observed in some clusters, and can also play an important role in the assembly of their galaxy population. Besides, the mass of the infalling structures appears to be tightly related to the kind of galaxy population that feeds the cluster. Nevertheless, it is still open to debate what are the relative contributions of these different inflowing scenarios. For instance, the *N*-body simulations of McGee et al. (2009) show that a significant fraction of the galaxies in a $z = 0$ cluster is absorbed from groups of galaxies, and that higher mass galaxies come from massive groups. In contrast, Berrier et al. (2009) indicate that the bulk of mass accretion in a cluster comes from *field* galaxies. In both scenarios, the infalling galaxies will be subjected to external conditions which can potentially modify their original properties like morphology, size and luminosity: *ram* pressure, galaxy harassment, merging, tidal stripping, etc. These phenomena can induce star formation, quench star formation by depleting the galaxies from their gas, modify the original properties of the galaxy components, lower or rise the mass of the galaxies and even create new galaxies from the debris of part of the infalling population (Park & Hwang 2009). The relative efficiency of all these will determine the overall effect of the mass growth of the cluster on the properties of the underlying population and will leave impressions on its luminosity function (LF) and morphological mix. Therefore, detecting, quantifying and analysing the properties of substructures in galaxy clusters, their overall shapes and the morphological properties of the cluster members are of extreme importance to understand the processes that drive the large-scale structure growth and formation.

Rembold & Pastoriza (2007, hereafter Paper I) have used multi-object spectroscopy (MOS) to analyse the kinematics and stellar population properties of a number of galaxies in the cluster LCDCS-S001, at $z = 0.709$. We have shown that the stellar population of the cluster members can be well described by solar metallicity templates, and that the bulk of their stellar populations is between 3.0 and 7.0 Gyr old. We have found a trend, in the sense that more massive galaxies, and also the galaxies whose stars are older and single-aged, populate the cluster centre. In the hierarchical formation scenario of clusters of galaxies, this happens because the central galaxies presumably are those that consumed their gas first, while the peripheral objects were recently accreted and, in general, are still forming stars. Moreover, we have shown that LCDCS-S001 has an associated radio emission in the direction of its centre, suggesting that important dynamical effects are taking place in the core of this cluster. Therefore, LCDCS-S001 is a good candidate in which to search for substructures, structural signs of merging processes and morphological evolution of galaxies.

In this paper, we analyse i' and r' photometric properties of the galaxies in the field of LCDCS-S001, in order to derive information on its intrinsic physical structure and search for signs of accretion processes. Besides, we present improved kinematic parameters from new MOS observations. In Section 2, we present the observations and data reduction process. Section 3 presents the methodology used to detect sources in the i' and r' images, as well as the completeness tests and derivation of photometric parameters. We analyse the kinematics of the cluster in Section 4, and Section 5 presents the morphological properties of the galaxies in the direction of the cluster. We analyse the cluster structure in Section 6, and its LF in Section 7. Our conclusions are summarized in Section 8. Throughout the paper, we will use $H_0 = 71\,\mathrm{km\,s^{-1}\,Mpc^{-1}}$, $\Omega_\mathrm{M} = 0.27$ and $\Omega_\mathrm{V} = 0.73$.

2 OBSERVATIONS AND DATA REDUCTION

The observations of LCDCS-S001 have been carried out with the GMOS instrument attached to the Gemini South Telescope, in three different observation runs. The first (ID GS-2004A-Q-18) comprehends i' imaging, as well as MOS observations, which have been analysed in Paper I and Krabbe, Rembold & Pastoriza (2007). The second (ID GS-2005A-Q-41) comprehends r' imaging. We have used the filters *G*0326 and *G*0328, which correspond to the broad-bands r' and i' and cover roughly the rest-frame optical region of spectra with the previously estimated cluster photometric redshift of $z = 0.47$. The final (ID GS-2010A-Q-55) comprehends MOS observations of a new set of sources in the direction of the cluster.

The imaging instrumental set-up was chosen so that the images have a spatial binning of 2×2 pixel, which corresponds to a spatial resolution of $0.144\,\mathrm{arcsec\,pixel^{-1}}$. We have obtained three exposures with a total time of 300 s for the i' band. A longer exposure time was used for the r' imaging (485 s). The i' and r' images were obtained under seeing conditions of 0.29 and 0.92 arcsec, respectively.

The mask for the MOS observations was built using as reference the i' image. Previous photometric analyses (colour–magnitude diagrams, projected distance to the cluster centre, SExtractor stellarity index and bulge fractions – see Sections 3 and 5) helped us to select 20 bright objects with higher probability of being cluster members. Five expositions of 1550 s were obtained, allowing us to reach a signal-to-noise ratio higher than 3 for objects of magnitude $i' = 20$.

Data reduction of the i' and r' images was based upon the co-added, pre-calibrated images made available by the Gemini staff. The three individual exposures were bias-corrected, flat-fielded, mosaicked and combined with the standard routines of the IRAF/GEMINI/GMOS package. Standard stars observed in the same nights were used for a photometric calibration of the sources extracted from the images. The MOS observations have been reduced by the same methodology as in Paper I: bias-corrected, flat-fielded and wavelength-transformed 2D spectra have been extracted in each fibre and the sky level was estimated by the peripheral light contribution of the fibre.

3 OBJECT DETECTION AND PHOTOMETRY

We have used the SExtractor software (Bertin & Arnouts 1996) to detect sources in the field images. SExtractor was conceived specifically for use in large surveys, such as high-redshift fields and galaxy clusters. It identifies individual sources by searching for groups of connected pixels with counts above a specific threshold in relation to the background fluctuation, and generates a catalogue with coordinates, magnitude and other useful parameters for each detected source.

A successful run of SExtractor requires a careful choice of its many configuration parameters. Among these parameters, the *thresholding* and the *deblending* parameters are of particular importance, since they define the sensitivity of the software to associate fluctuations above the background to a source and the extent to which it will try to fragment a blended source in separate objects. Many authors have set these parameters to values such that *no detection* is made on the *negative* image of the field (Chen et al. 2002; Rafelski et al. 2009). We have chosen a less strict criterion, similar to that of Shim et al. (2006). We have made several runs with SExtractor with different parameters, and analysed the resulting detections by eye. We have then set the parameters so that almost

all sources that could be detected by eye were correctly detected and deblended from sources in their vicinity, and the number of spurious detections was the lowest possible, as shown in Fig. 1. The best performance was achieved for `DETECT_MINAREA` = 10, `DETECT_THRESH` = 1.5 and `DEBLEND_MINCONT` = 0.01. Spurious objects were detected mainly at the periphery of the image, where the noise is higher. The mesh size of background determination was set to 128 pixels.

As the i' image was obtained under good atmospheric conditions (seeing of 0.29 arcsec), this image was used for the detection of objects with SExtractor, for deriving astrometric parameters, as well as the apparent i' magnitudes and the stellarity index of each source. To obtain the $r' - i'$ colour, we have degraded the i' image to match the seeing full width at half-maximum (FWHM) of the r' image, by convolving it with a point spread function (PSF) with FWHM = 0.87. We then made a second run of SExtractor in dual-image mode, using the i' image as source. The magnitudes (and colours) obtained and referred throughout this work are the `MAG_BEST` calculated by SExtractor. The raw catalogue of sources generated by SExtractor for the i' image comprehends 3717 sources, of which only a selected sample will be analysed in the present paper. Our final catalogue consists of the 901 non-stellar objects (sources with SExtractor stellarity index inferior to 0.8) brighter than $i' = 25.0$, which were successfully fitted by the gim2d (see Section 6). For most of these objects, a fit was also successfully obtained with galfit (see Section 6). The $r' - i'$ colour is available for a fraction of the sources. Each object in the catalogue has an identification composed by a running number from 1 to 901; many objects have also a second identification number, based on a preliminary list of 545 candidate sources for spectroscopy and referred to in Paper I.

3.1 Completeness of the photometric sample

Sample completeness has been estimated through the analysis of a number of synthetic sources built on a pre-selected and pre-cleaned section of the i' image. Extended sources with luminosity profiles following bulge+disc laws for several bulge fractions and apparent magnitudes, as well as sources with stellar profiles, were generated using the iraf/noao package artdata. We have run SExtractor on this image section and the success rate of identification and extraction of objects was determined. Fig. 2 shows the results for different surface densities of sources (more or less crowded fields). For a surface density of 57.6 object arcmin^{-2}, typical of the source density in the i' image, only 10 per cent of the objects with $i' = 25$ were detected. Even for brighter objects, crowding of sources causes more than 10 per cent of the sources to be missed. We have fitted a selection function $P(i')$ to the data of the form

$$P(i') = \frac{a}{1 + (i'/b)^c}, \quad (1)$$

where a is the maximum per cent detection rate, b is the magnitude at which $P(i')$ reaches 50 per cent and c indicates the slope of the detection rate curve. Our best-fitting function was found when $a = 82.12$, $b = 24.04$ and $c = 50.80$. This selection function is also shown in Fig. 2. This function shows that our photometric sample is 50 per cent complete at $i' = 24$. It was used to correct all derived parameters that are sensitive to contamination by foreground and background galaxies.

4 REDSHIFTS AND KINEMATICS

We have obtained the redshift of the galaxies in our sample by direct identification of spectral features and calculation of the line shifts. This simple method is similar to that used in Paper I and was chosen because in many spectra telluric features are present even after sky subtraction, and they mimic high correlation peaks in cross-correlation methods. Table 1 shows the redshifts and coordinates of all 22 confirmed cluster members (see below), of which 12 have been presented in Paper I. Fig. 12 shows the projected distribution of the confirmed cluster members in the cluster field.

In order to determine the median redshift of the cluster and its velocity dispersion, we have used the biweight estimator (Beers, Flynn & Gebhardt 1990). We have obtained $z = 0.7083$ (a little less than previously determined) and $\sigma = 887 \pm 249\,\mathrm{km\,s^{-1}}$, with

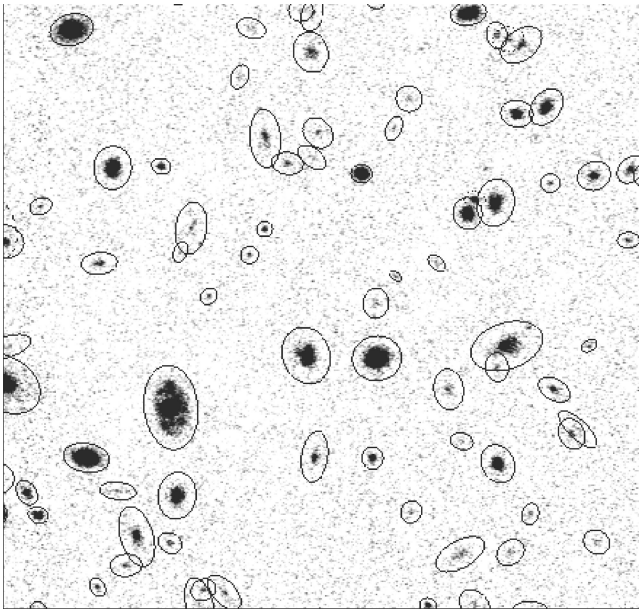

Figure 1. Section of 1 × 1 arcmin^2 on the i' image showing the sources detected by SExtractor.

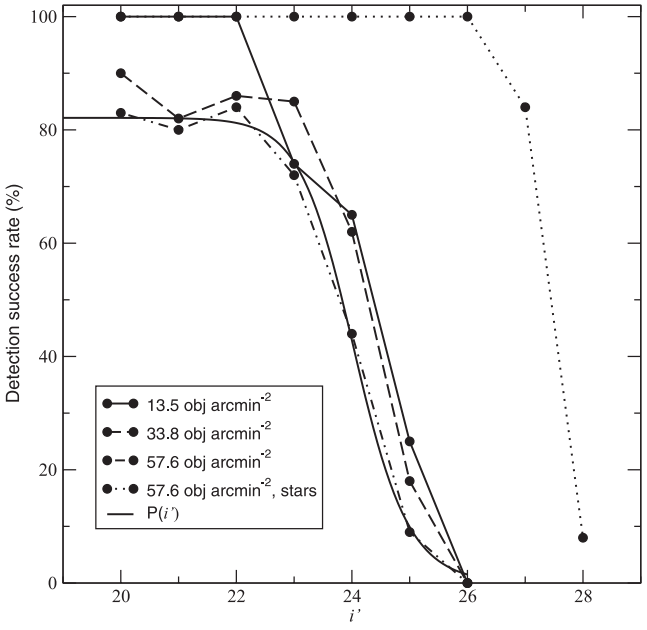

Figure 2. SExtractor source detection success rate versus magnitude source for different source densities.

Table 1. Redshifts and coordinates of the confirmed cluster members.

ID	z	RA (2000) ($^{h\,m\,s}$)	Dec. (2000) ($^{\circ}\,'\,''$)
302	0.7090	10 06 24.77	−12 57 10.2
226	0.6983	10 06 20.94	−12 57 35.5
318	0.7077	10 06 19.46	−12 57 04.0
224	0.7091	10 06 21.20	−12 57 35.5
1481	0.7107	10 06 20.30	−12 58 36.7
236	0.7173	10 06 19.70	−12 58 23.9
157	0.7074	10 06 18.37	−12 59 11.6
244	0.7093	10 06 18.45	−12 58 32.9
175	0.7064	10 06 16.17	−12 59 06.9
182	0.7086	10 06 14.71	−12 59 50.1
273	0.7055	10 06 13.51	−12 58 23.1
241	0.7090	10 06 18.69	−12 58 21.0
885	0.7093	10 06 20.76	−12 59 18.6
270	0.7068	10 06 18.91	−12 58 12.9
166	0.7076	10 06 22.18	−12 58 24.4
793	0.7145	10 06 21.76	−12 59 44.4
1	0.7083	10 06 19.20	−12 59 17.5
83	0.7106	10 06 23.07	−12 58 40.2
395	0.6951	10 06 16.33	−12 57 47.2
238	0.7097	10 06 17.87	−12 58 25.7
77	0.7092	10 06 15.39	−12 59 15.3
350	0.7032	10 06 12.05	−12 58 17.3

a total of 22 confirmed members. This agrees very well with our previous estimate of $\sigma = 727 \pm 185\,\mathrm{km\,s^{-1}}$ in Paper I. A simple virial analysis as presented, e.g., in Girardi et al. (1998) gives a virial radius $R_{200} = 0.98 \pm 0.22\,\mathrm{Mpc}$ and a mass of $M_{200} = (5.4 \pm 2.8) \times 10^{14}\,\mathrm{M_{\odot}}$, which also agree well with our prior estimates.

5 STRUCTURAL PARAMETERS AND MORPHOLOGY OF THE GALAXIES IN THE PHOTOMETRIC SAMPLE

The structural parameters of the extended sources of our raw catalogue have been derived with the softwares GIM2D (Simard 1998) and GALFIT (Peng et al. 2002). GIM2D was developed for the IRAF ambient. It reads as input a catalogue of sources, finds each source in the reference image, and derives its structural parameters (bulge+disc decomposition). GALFIT is a flexible software which fits diverse 2D brightness profiles, like PSFs, spiral arms, edge-on disc profiles, bulges and discs. We have run both GIM2D and GALFIT on the i' image and used as input the sources detected by SExtractor in this image. The output of these softwares is the structural parameters, like the effective radius of the bulge and the scale radius of the disc (r_e and r_d), their position angles and inclinations. As the set-ups of these two softwares are different, as well as their limitations and strengths, we have used a particular configuration for each.

GIM2D is sensitive to a number of configuration parameters. In particular, the user can choose to let GIM2D determine the sky level at the galaxy position (setting *dobkg* = *yes*), or to fix a sky level provided externally. Also, the user can limit the parameter space which will be tested by GIM2D (setting *initparam* = *yes*); this is particularly useful if one wishes to lower the time GIM2D takes to reach convergence. Simard (1998) suggests that the best results are obtained with both *initparam* and *dobkg* set to *yes*. On the other hand, Häussler et al. (2007) have shown that GIM2D produces biases in the fit of 2D Sérsic profiles, in the sense that faint galaxies show both a systematic lowering of the Sérsic index and an increase in magnitude, and suggest that the best performance of GIM2D is reached for an external, fixed, sky determination, and with *initparam* = *no*. Hoyos et al. (2011) have found that the systematic bias is not as large as found by Häussler et al. (2007) and chose a slightly different best configuration for GIM2D: enlarging the mesh size for background determination on SExtractor and setting GIM2D to *dobkg* = *no*. This wide background mesh is reasonable for *Hubble Space Telescope* images but not feasible for ground-based photometry, because of the strong sky background influence, as large background meshes make the sky estimation less sensitive to local sky variations. Therefore, once we are interested in bulge+disc decompositions (a different 2D fit as the one tested by Häussler et al. 2007), we have decided to run GIM2D as suggested by Simard (1998) and to perform tests with simulated galaxies in order to evaluate eventual biases.

While both GIM2D and GALFIT can fit bulges with a Sérsic profile, we have chosen to run GALFIT with a fixed $n = 4$. We did this because GALFIT requires much more interaction with the user, specifically in the choice of initial parameters – a bad choice usually makes the estimated GALFIT values for each iteration to diverge, making the software to stop making new iterations and unable to achieve a valid solution. While a careful, individual choice of starting parameters for a given galaxy can be easily made if one wants to fit the 2D brightness distribution of a handful of galaxies, it is too time consuming for large samples of galaxies as ours. In our preliminary tests with GALFIT, we observed that fixing the bulge's Sérsic improves its performance a lot. We have used multiples of the square root of the isophotal radius as first guesses of radial scale of the bulge and the disc; this choice usually led the software to the correct ones in our preliminary tests. The most critical of our first guesses was the relative magnitude of the bulge and the disc. While GALFIT is able to handle magnitudes wrong by ∼1 mag, it frequently gets locked in local minima with magnitudes differing more from the correct ones than 1.5–2 mag. In order to circumvent this problem, we have run GALFIT five times for each object, with magnitude differences of 1 and 4 units in both directions (brighter bulge and brighter disc) and with equal magnitudes for both components; the fit with lowest χ^2 among these five runs was chosen as the best fit. Though this methodology does not prevent GALFIT from diverging the parameter values while searching for minima, it did improve its performance sensibly.

In order to test possible biases and the general performance of GIM2D and GALFIT as applied to our data, we have generated mock images of the cluster with the IRAF package ARTDATA. A number of extended sources similar to that found in our image (as extracted by SExtractor) were created in an image with background level, read-out noise and gain matching those of our science images. As extended sources, we have added pure bulges ($R^{1/4}$) and composite bulge+disc galaxies, with arbitrary bulge fractions. We have run GIM2D and GALFIT on the mock image with the same parameters as used in the science images and compared it to the input parameters of the simulated galaxies.

Figs 3–5 show our findings. In Fig. 3, one can see that both codes systematically overestimate the galaxy magnitudes, and this trend becomes stronger for higher magnitude galaxies. For GALFIT, the overestimate in general does not exceed 0.2 mag at $m = 24$ mag, but GIM2D produces a much higher overestimate, even for brighter objects. Fig. 4 shows the B/T values derived with GIM2D and GALFIT and compared to the model ones. While the GALFIT values clearly show a correlation with the model B/T values, for GIM2D a much poorer correlation is obtained. The strongest correlation is seen for quasi-bulgeless systems, for which GIM2D in general reproduces low B/T values; bulge-dominated systems are given B/T values by GIM2D

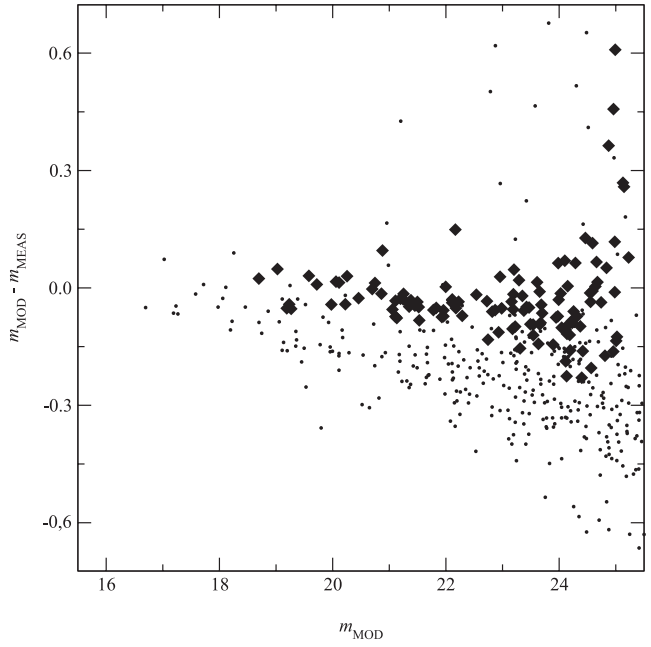

Figure 3. Relation between the model (m_{MOD}) and measured (m_{MEAS}) magnitudes as obtained with GALFIT (black diamonds) and GIM2D (black dots).

which look even arbitrary. Fig. 5 shows that the correlation between model and measured *B*/*T* values is strongly dependent on the source magnitude. In this figure, we plot only objects with $m < 24$ mag. Note that in this figure the correlation between model and measured values is much stronger, but for GALFIT it is much better defined than for GIM2D. Both follow the approximate relation

$$B/T_{MEAS} \approx 0.76\, B/T_{MODEL}. \quad (2)$$

The differences between model and measured *B*/*T* values can be seen also in a *B*/*T* histogram, as shown in Fig. 6. Both GIM2D and GALFIT are unable to reproduce the model *B*/*T* histograms, but while GALFIT mainly dilutes pure bulge systems among lower *B*/*T* values, GIM2D seems to *invert* the original distribution, assigning more occurrences for low *B*/*T* galaxies in a sample rich in bulge-dominated objects. Finally, selecting only objects with $m < 24$ mag (the data from Fig. 5) and correcting the measured *B*/*T* values with equation (2), we obtain the *B*/*T* histograms shown in Fig. 7. This figure shows a much better reproduction of the original values of *B*/*T* for both GALFIT and GIM2D, though GIM2D shows larger deviations especially for high *B*/*T*. While the individual bins generally do not match, the global *B*/*T* distribution is similar.

Finally, the automated estimates of *B*/*T* also suffer selection effects, because both GALFIT and GIM2D produce solutions more or less stable for different *B*/*T* values. This effect can be seen qualitatively in Fig. 4: for the same input (artificial) galaxy population, the number of successful fits is much higher for GIM2D than for GALFIT. GALFIT, for some reason, failed much more frequently to find a solution for disc-dominated galaxies, and the uncertainties in the *B*/*T* values found with GIM2D were in general larger – sometimes, prohibitively large – for disc-dominated than for bulge-dominated objects. This behaviour produces a bias in the final sample and underestimates the fraction of low *B*/*T* systems. Therefore, for an input galaxy population drawn from a 'flat' *B*/*T* histogram, both routines will produce a constantly rising distribution; around half of the galaxies with low *B*/*T* values will be lost. We have evaluated

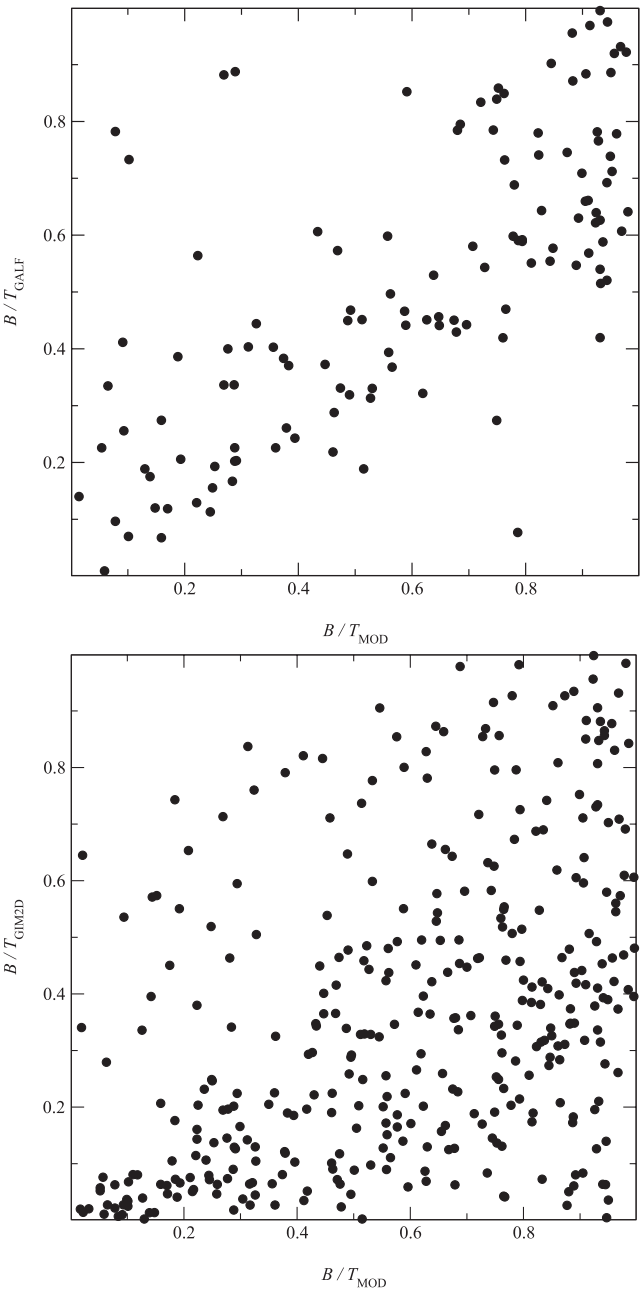

Figure 4. Relation between the model *B*/*T* values and those obtained with GALFIT (upper) and GIM2D (lower).

the intensity of this bias in the simulated sample for each *B*/*T* range, and in the following analysis we take this into account.

In order to analyse the morphologies of the galaxies in the cluster, we have calculated the number of galaxies in bins of *B*/*T* with width 0.1, both inside and outside R_{200}. The resulting distributions were then corrected for the biases discussed in Section 5, and the cluster distribution was obtained by the rescaled difference of the number counts inside and outside R_{200}. Fig. 8 shows the histograms of the relative contribution of *B*/*T* values for the cluster galaxies and field galaxies, obtained with GALFIT and GIM2D. We can see that the galaxies in the sample tend to low *B*/*T* values.

In order to make inferences about the morphological mix in the cluster, we have defined discriminating values of *B*/*T* in order to split the sample in morphological types. A separation among the many

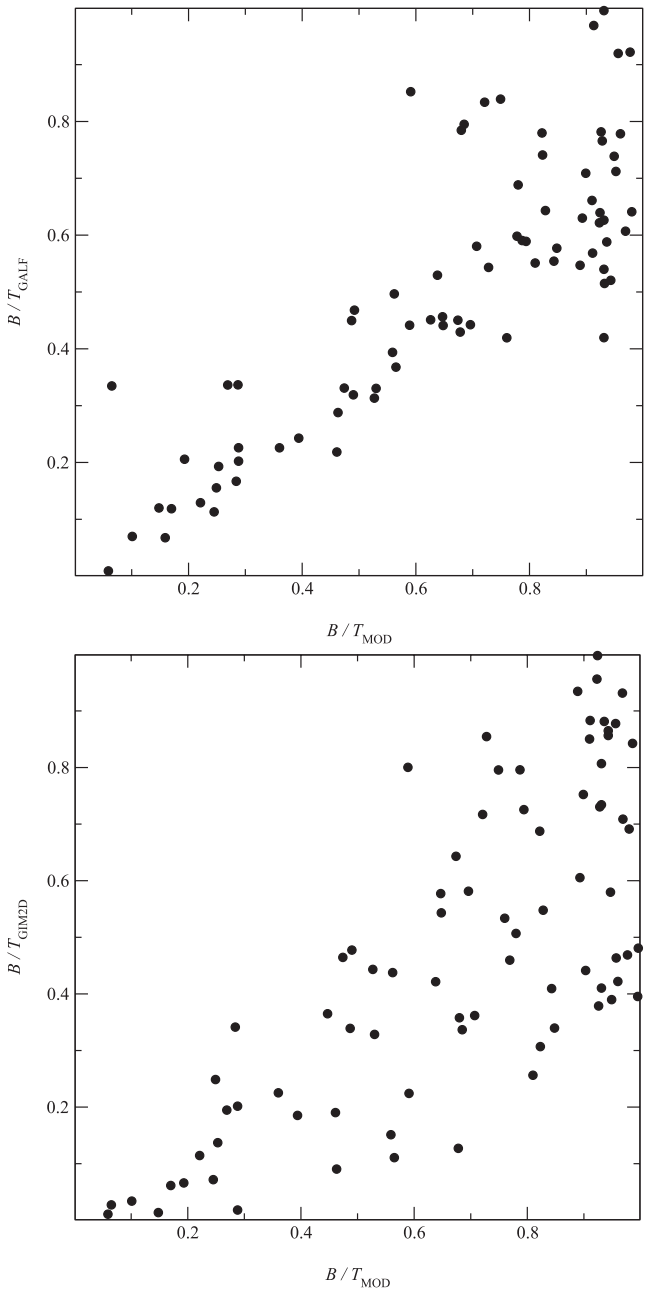

Figure 5. *B*/*T* values obtained with GALFIT (upper) and GIM2D (lower) for $m < 24$ mag objects as a function of the model values.

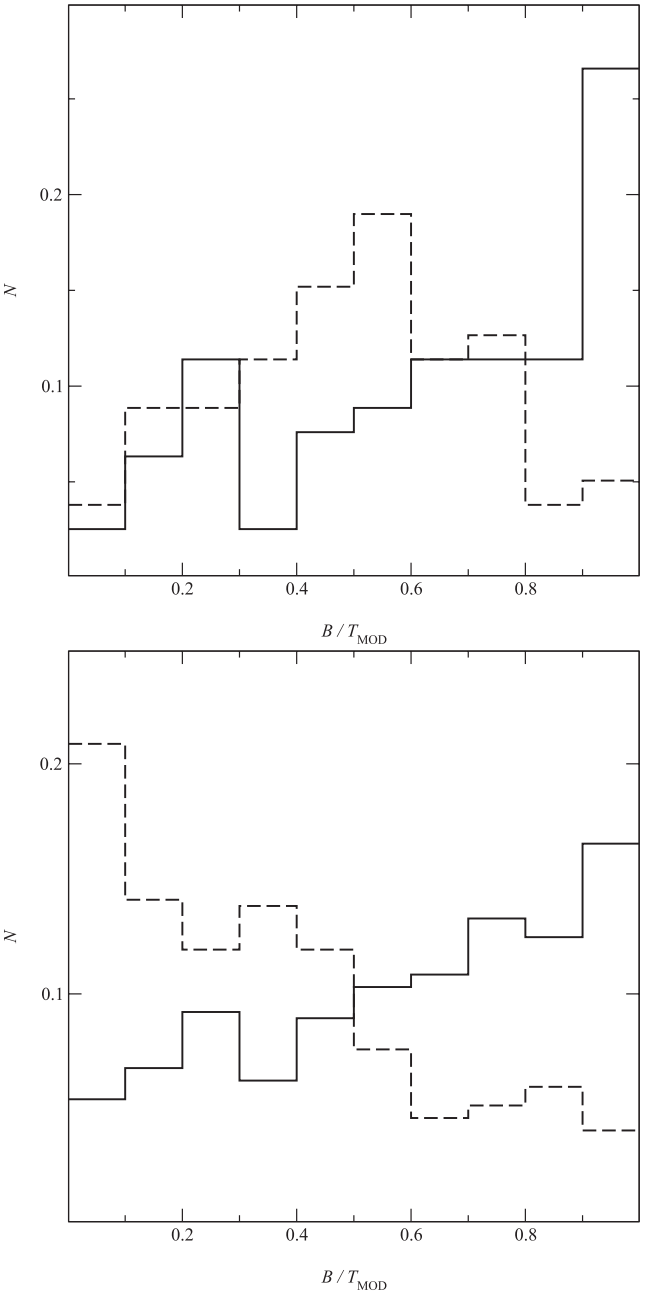

Figure 6. *B*/*T* histogram obtained with GALFIT (upper) and GIM2D (lower) and compared to the model ones. The solid line indicates the model histogram, and the dashed lines show the measured values.

morphological types relies on the assumption that *B*/*T* has a one-to-one correspondence with the morphology of each galaxy, which is not true. This means that, whatever the choice of the discriminating values, any subsample of *B*/*T* values will not, strictly speaking, represent any one morphological type. Besides, late-type and early-type galaxies comprise different morphological types and the independent *B*/*T* distributions of each type are not easy to disentangle. So, we have limited ourselves to define a single discriminating *B*/*T* value to separate bulge- and disc-dominated galaxies. Different discriminating values have been used in the literature. Cheng et al. (2011), for example, use the value $B/T = 0.6$. Applying this value to our distribution, we find that 73 ± 13/67 ± 7 per cent of the galaxies in the sample are disc dominated (with GIM2D and GALFIT, respectively). Tran et al. (2001) use a discriminating value $B/T = 0.4$ to separate early types (E+S0) from spirals. These authors discuss the validity and meaning of this choice. If we compare this value with that of Cheng et al. (2011) and their fig. 5, it seems that this value really separates the bulk of early types ($B/T > 0.4$), but a large fraction of discs will be lost to the early-type population. Our findings, therefore, no matter the values chosen to separate the classes, must be seen with caution. Using the discriminating value $B/T = 0.4$, we find that 46 ± 3 and 54 ± 4 per cent of late-type galaxies in LCDCS-S001, as determined with GIM2D and GALFIT.

Lubin et al. (1998) found that, for clusters at $z \sim 0.8$–0.9, the morphological mix varies strongly among different systems, from 76 per cent of early types in a high-mass cluster to fractions typical

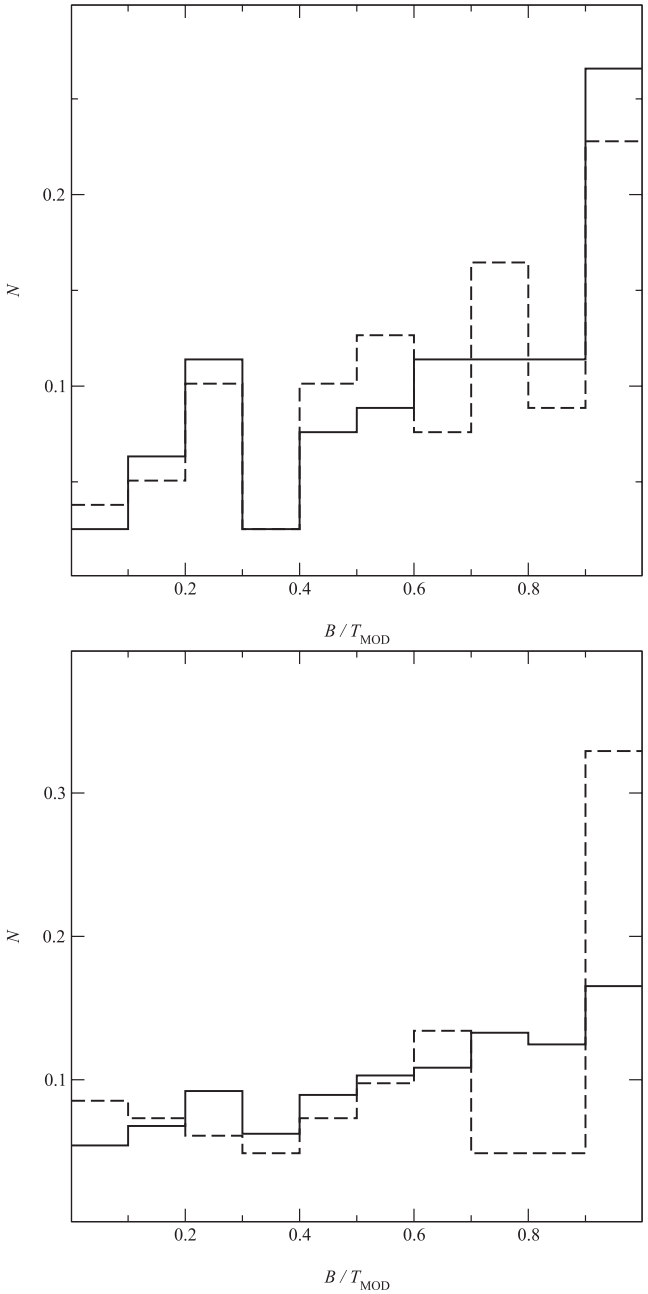

Figure 7. Corrected *B*/*T* histograms for GALFIT (upper) and GIM2D (lower) and compared to the model ones. The meaning of the lines is the same as in Fig. 6.

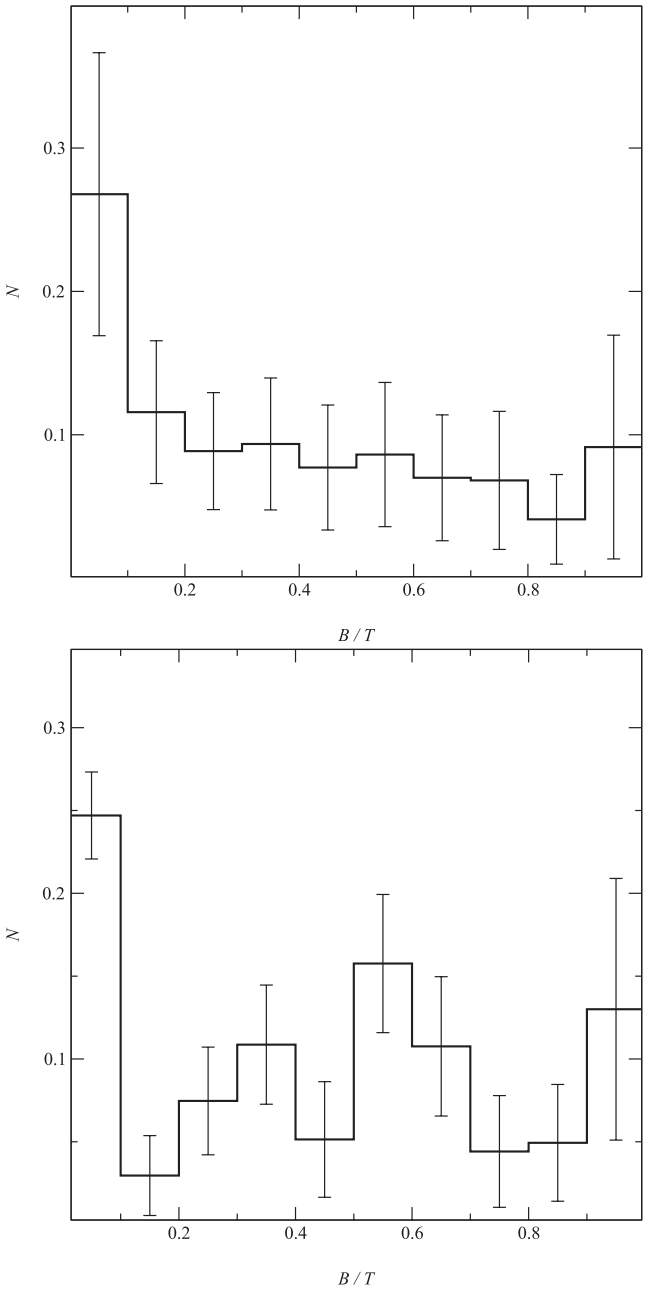

Figure 8. *B*/*T* histogram of the cluster galaxies.

of the field for a lower mass one, at least for the central 0.5 Mpc. Lubin, Oke & Postman (2002) have found a fraction of early-type galaxies of 55 per cent for a rich cluster at $z \sim 0.76$; note that this value is very similar to the ones we obtain with a discriminating value $B/T = 0.4$. van Dokkum et al. (2000) have also found that the early-type fraction in rich clusters is lower at higher redshift, reaching around 50 per cent at $z \sim 0.7$ (see their fig. 6); a similar value was obtained by Simard et al. (2009) at this redshift. Comparing clusters with different dispersion velocities, Poggianti et al. (2009) found that, at $0.5 < z < 1.2$, the spiral fractions of high and low velocity dispersion systems are 40 and 60 per cent, respectively. Our data are, therefore, compatible with other determinations of the early-type fractions of rich clusters at high redshift and reinforce the view that the morphological mix in clusters of galaxies has evolved strongly over at least the latter half of the cosmic time. Once the fraction of elliptical galaxies does not seem to depend on redshift, our data are therefore a natural extension of the relation found by Fasano et al. (2000) and Just et al. (2010): late-type cluster galaxies at $z \sim 0.7$ are overabundant and are the probable progenitors of the present-time S0 population.

In the above analysis, we have used a PSF modelling using a Moffat profile with $\beta = 1.5$, which produced the lower residuals in our preliminary tests with GIM2D. However, variations of the FWHM of the PSF between the exposures and along any one exposure will have an impact on the derived best-fitting parameters of the sample galaxies. A full analysis of this effect would require a whole series

of GALFIT/GIM2D runs for different PSFs applied to the artificial fields, a very time consuming procedure. As an estimate of the impact of PSF mismatch, we have run GIM2D and GALFIT on a subsample of six objects from our mock sample, for different PSFs with widths varying from 10 to 50 per cent larger than the original value of the nominal FWHM. We have found that this mismatch biases the *B*/*T* values originally fitted with both GIM2D and GALFIT to intermediate ones. This presumably happens because it is easier to fit a model with the 'wrong' PSF on the brightness distribution of a galaxy with a combination of two components than with only one. Variations of up to 15 per cent in *B*/*T* have been found, what implies that, in our *B*/*T* histograms, a given galaxy could be located up to two bins closer to the 0.5 value than it would be without PSF mismatching. While this effect surely affects the overall *B*/*T* distribution and lowers the population of the extreme bins (*B*/*T* ~ 0 and ~ 1), our results concerning the morphological mix would not be strongly affected, because our discriminating values for early and late types are close to 0.5.

6 CLUSTER PROJECTED STRUCTURE

Probing the physical structure of galaxy clusters based purely on photometric observations constitutes a challenge, not only because of projection effects on the intrinsic cluster structure but also because of the difficulties in identifying the cluster members and segregating them from background and foreground galaxies and extended structures. The number of confirmed cluster members in our analysis (22) is insufficient to derive details on the physical structure of the cluster. In what follows, we will try to use the photometric information to infer hints on the cluster physical structure.

6.1 Analysis of the projected distribution

In order to investigate the projected density of objects in the cluster, we have defined a density parameter *A*, which corresponds to the sum of the average object densities in several rings of radius *r* and thickness Δr. For a specified value of Δr around a given centre, it is expressed by

$$A = \sum_{i=1}^{m} \frac{N_i\,(i\,\Delta r) - N_{i-1}[(i-1)\,\Delta r]}{\pi\,(i\,\Delta r)^2 - \pi\,[(i-1)\Delta r]^2}, \quad (3)$$

where *m* defines the maximum calculation radius, *i* is the ring index and N_i is the number of objects contained in all rings up to ring *i*. This parameter is more sensitive to density fluctuations near the centre of calculation than in more peripheral rings. Fig. 12 shows the 2D distribution of the *A* parameter for $\Delta r = 100$. The details of this distribution will be analysed below. The relative distribution of *A* is not heavily influenced by the choice of Δr, and the peak value of *A* occurs for nearly the same region in the image, irrespective of Δr. We have then used the peak *A* value to define a distribution centre. The average value was found to be $\alpha(\mathrm{J2000}) = 10^{\mathrm{h}}06^{\mathrm{m}}18\overset{\mathrm{s}}{.}9$, $\delta(\mathrm{J2000}) = -12^{\circ}58'29\overset{''}{.}4$. Throughout this paper, these coordinates will be considered the projected coordinates of the cluster centre.

6.1.1 *Cluster shape*

The most immediate property seen in Fig. 12 is the elongated morphology of the cluster, in the south–north direction. In order to characterize the ellipticity and the orientation of the cluster, we have applied two complementary methods: (i) the tensor of inertia method of West, Dekel & Oemler (1989) and (ii) simulation of cluster fields with different properties, which we compare directly to our data. The method of West et al. (1989) is a principal axis method; the components $I_{i,j}$ of the tensor of inertia are defined as

$$I_{i,j} = \sum_k \frac{x_i x_j}{r^2}, \quad (4)$$

where $x_1 = x, x_2 = y$ are the coordinates of the *k*-th galaxy and $r = \sqrt{x_1^2 + x_2^2}$. The ellipticity and the position angle of the semimajor axis of the cluster are then

$$\varepsilon = 1 - \frac{\Lambda_{\min}}{\Lambda_{\max}} \quad (5)$$

and

$$\phi = \tan^{-1}\frac{\Lambda_{\max} - I_{1,1}}{I_{1,2}}, \quad (6)$$

where

$$\Lambda_{\min} = \frac{I_{1,1} + I_{2,2}}{2} - \frac{1}{2}\sqrt{(I_{1,1} + I_{2,2})^2 - 4(I_{1,1}I_{2,2} - I_{1,2}I_{2,1})}. \quad (7)$$

We have applied this method to our sample galaxies in different radii from the cluster centre. Our results are summarized in Fig. 9. Except for the region between 300 and 400 kpc, where both parameters are affected by the presence of a local overdensity, the position angle is stable around $\sim -50^{\circ}$, while the ellipticity, after reaching a peak of $\varepsilon \sim 0.6$, falls to $\varepsilon \sim 0.3$. The fall in the cluster ellipticity is due in part to the rising proportion of field galaxies. This and other limitations of ellipticity estimators in general, including the tensor of inertia method of West et al. (1989), have been noted, e.g., by Rhee, van Haarlem & Katgert (1989) and de Theije, Katgert & van Kampen (1995). In particular, de Theije et al. (1995) argued that, in the presence of background galaxies in the sample, the method underestimates the real ellipticity of the cluster. In order to test the effect of background contamination on this method, we have simulated clusters of galaxies whose radial number profile follows

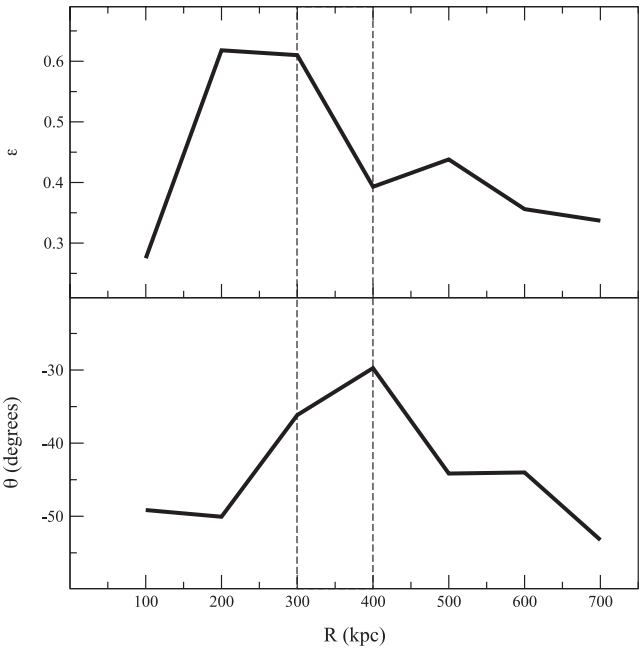

Figure 9. Radial dependence of the ellipticity (top) and position angle (bottom) of the semimajor axis of the cluster, as determined by the tensor of inertia method of West et al. (1989). The region between 300 and 400 kpc, contaminated by a local overdensity, is indicated by vertical dashed lines.

the analytical approximation of the isothermal sphere profile given below, with varying ellipticities ($\varepsilon = 1 - b/a$), core radii (R_C) and total number of objects:

$$N(R) = \frac{N_0}{1 + [R(\theta)/R_C]^2}, \tag{8}$$

where

$$R(\theta) = \frac{a\sqrt{1-\varepsilon^2}}{\sqrt{\sin^2(\theta-\theta_0) + (1-\varepsilon^2)\cos^2(\theta-\theta_0)}}, \tag{9}$$

and θ_0 is the orientation of the semimajor axis a of the ellipse. Background galaxies with random positions were added to the simulations, so that the total number of galaxies always matches the size of our photometric sample. In all simulations, we have kept the orientation of the semimajor axis of the cluster to -50°. Applying this method to our galaxies, we have obtained the data shown in Fig. 10. We note that, even without background galaxies, the method overestimates the ellipticity for very round systems and tends to underestimate it somewhat for flatter systems. The addition of background galaxies produces an overall underestimate of the ellipticity; the intensity of this effect is stronger when the background level is higher. A measured value of $\varepsilon \sim 0.3$ can be obtained for clusters with 'real' ellipticities from $\varepsilon \sim 0.4$ to $\sim$0.9 for different background levels. Once we do not have a direct estimate of what fraction of our photometric sample belong to the cluster, we cannot correct the measured ellipticity of our cluster with this method. On the other hand, the position angle of the cluster semimajor axis is very well reproduced irrespective of the background level: we found around 75 per cent of the measured orientations within 10° of the real orientation of the simulated cluster.

We have determined the radial distribution of galaxies in the cluster by simulating realizations of density profiles given by equation (8) with different core radii, total number of objects and ellipticities, using as the only fixed parameter the orientation of the semimajor axis to match that found with the method above. We have allowed the core radii to vary from 10 to 490 kpc, the ellipticity from 0.00 to 0.95 and the total number of cluster galaxies from 10 to 500. In order to verify which simulations best represent the distribution of galaxies in LCDCS-S001, we have measured the galaxy counts in five annuli around the cluster centre, and in four angular bins, for each simulation and determined the squared difference between these counts and the observed one. The region of the three-parameter space which minimized this squared difference was chosen as the best-match distribution. With this method, we have obtained the best agreement with a model with $N = 214 \pm 73$, $R_C = 283 \pm 66$ kpc and $\varepsilon = 0.49 \pm 0.14$.

In order to check the validity of our method, we have also applied it to a sample of 40 simulated clusters, with ellipticities, core radii and member galaxies spanning all our parameter space. Fig. 11 shows that our determinations fit very well the properties of the simulated clusters. The best reproduced parameter is the core radius of the distribution. The total number of galaxies is well determined up to $N \sim 300$, above which it becomes noisy, because a larger volume in the parameter space becomes compatible with these distributions. As for the ellipticity, a small trend towards smaller (larger) values is observed for clusters with $\varepsilon > 0.2$ ($\varepsilon < 0.2$), but the discrepant clusters also have larger errors.

Comparing Figs 10 and 11, we note that both methods give coherent results for the ellipticity. Fig 11 shows that our value $\varepsilon = 0.49 \pm 0.14$ probably reflects the correct one or is a slight underestimate of the real value. Fig 10 shows that for a cluster with $N \sim 300$ and $\varepsilon \sim 0.5$, a value $\varepsilon \sim 0.3$ can be obtained via tensor method, a value compatible with the one we have found for LCDCS-S001.

The value $\varepsilon = 0.49 \pm 0.14$ means that LCDCS-S001 is more elongated than the average clusters at low redshift. Struble & Ftakas (1994) have found an average value of 0.35 ± 0.10 for clusters with $2.8 < \log\sigma < 3.0$ at $z = 0$. Several authors (Rahman et al. 2006; Biernacka, Flin & Panko 2009; Plionis, Tovmassian & Andernach 2009) have detected a redshift evolution of the ellipticity of clusters at least to $z \sim 0.18$, in the sense that higher-z clusters tend to show higher ellipticity. This can be understood if we are witnessing earlier periods of the dynamical evolution of clusters of galaxies for higher redshifts. Plionis (2002) has found, for galaxies in the range $0.00 < z < 0.17$, an average value $\varepsilon \sim 0.4$, but with large scatter. Biernacka et al. (2009) have found 0.23 ± 0.12 for clusters at $z < 0.08$ and 0.32 ± 0.15 for $z > 0.16$. Panko et al. (2009) have found values ranging from 0.34 ± 0.14 to 0.18 ± 0.08 for low/high-mass (high/low-redshift) systems. The flatness of clusters of galaxies has been interpreted in terms of virialization and secondary infall, and N-body simulations have been carried in order to study the shapes of

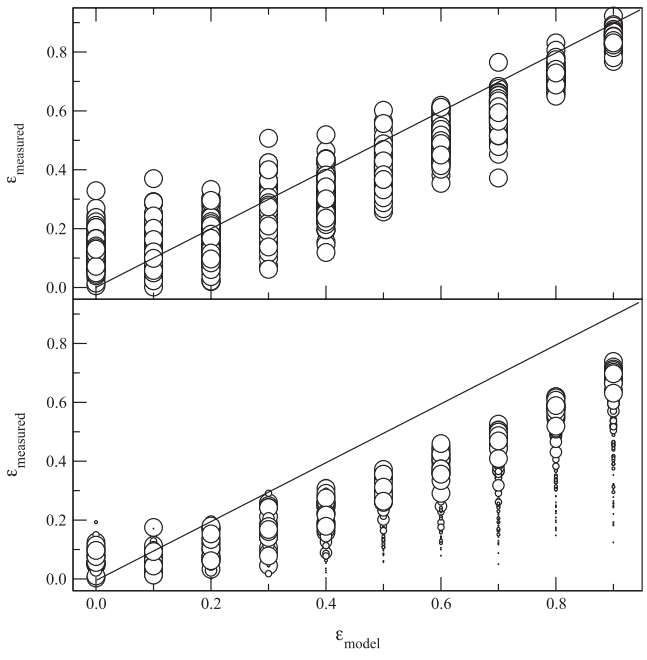

Figure 10. Ellipticity determined by the tensor of inertia method for our simulated clusters. The top diagram shows the ellipticity determined without background galaxies, and the bottom diagram shows the measured ellipticity with different fractions of background galaxies (the size of the circle is proportional to the fraction of background galaxies). The diagonal line indicates the perfect match locus.

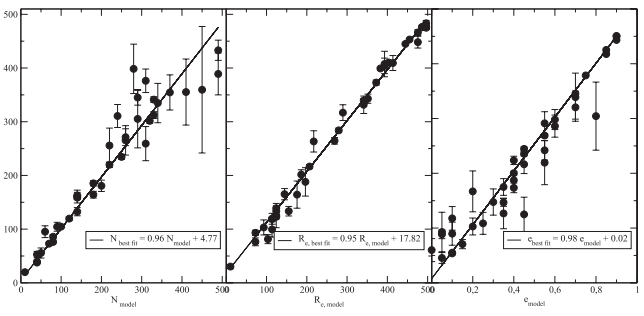

Figure 11. Comparison between the simulated cluster properties and the estimated ones.

clusters of galaxies and to use it as a cosmological tool. For example, Hopkins, Bahcall & Bode (2005) have made *N*-body simulations and found larger projected ε values for large mass high-redshift systems: for $z \sim 0.7$ and $M > 10^{14}\,M_{\odot}$, $\varepsilon \sim 0.42$. The high value found for LCDCS-S001 shows that this trend extends at least to $z \sim 0.7$ and suggests that LCDCS-S001 is still dynamically young.

The core radius found for LCDCS-S001 is very similar to the median value found for high-redshift clusters in Strazzullo et al. (2005). Also, it is in qualitative agreement with the relations between the virial radius and the core radius of Girardi et al. (1995, see their fig. 1b). Strazzullo et al. (2005) have found that core radii between 100 and 500 kpc 'refer to clusters which are generally single-peaked, but exhibit some broader asymmetric overdensity region or a filamentary structure', while clusters with smaller/larger cores are very regular/irregular, respectively.

6.1.2 *Cluster substructure*

The *A* parameter is sensitive to the local density of sources. Far from the centre of calculation, it dissolves any substructures in a wide ring with a certain thickness. If *A* is calculated in a region where the density of sources nearly equals the fore-plus-background density, its value will be low. So, we expect that the 2D distribution of *A* will show low and nearly constant values where the local density of galaxies matches that of the field (not related to physical associations of galaxies), and high values where the cluster structure overlaps the field. The most immediate feature seen in Fig. 12 is the elongated morphology of the distribution, reflecting the flattened morphology already discussed in the ellipticity determination. We can also easily see local density peaks, but by far the most prominent is the small and circular overdensity north-west of the cluster centre. The central *A* value of this local density almost reaches the density of the cluster centre; besides, this local density peak can be seen in the field image as notoriously decoupled from the vicinity, and at least one of the confirmed cluster members is situated in this region. Given the insulation of this region as seen in the density distribution, this region can be a semi-independent physical system like a group or a small mass cluster which is being absorbed by the main cluster.

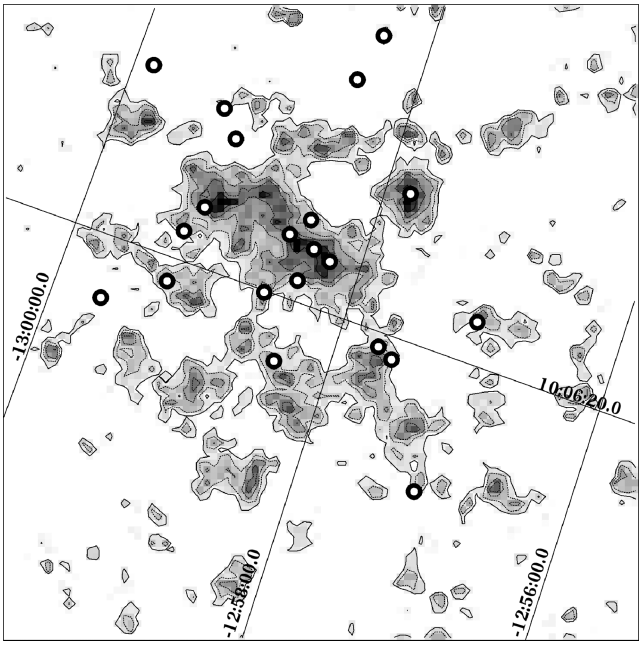

Figure 12. Projected density of sources in the cluster field given by the density parameter *A*. The image comprehends 5×5 arcmin^2. Circles represent the confirmed cluster members.

7 LUMINOSITY FUNCTION

We have determined the central cluster LF by counting the number of galaxies in specific magnitude bins, after correction for completeness and contamination from field objects. First, the total sample of galaxies was divided in bins of 0.5 mag, ranging from $i' = 21$ to 25. The number of objects per bin was then corrected for completeness, according to Section 3.1. We have then counted the number of objects inside a projected radius of 500 kpc and in four different external 'control areas'. These control areas will be used to correct the cluster LF by the field count contribution. With the naive supposition that the cluster LF is the same at any radial distance to the centre, the galaxy counts $N(m)$ in each bin of magnitude of the cluster LF would be given by

$$N(m) = N_{\rm INT}(m) - S_{\rm INT}\left[\frac{N_{\rm INT}(m) - K\,N_{\rm OUT}(m)}{S_{\rm INT} - K\,S_{\rm OUT}}\right], \qquad (10)$$

where $N_{\rm INT}$ and $N_{\rm OUT}$ are the total number of galaxies in the magnitude bin m inside $0.5\,R_{200}$ and in the control field, respectively, $S_{\rm INT}$ and $S_{\rm OUT}$ are the areas of these image sections, and K is the fraction of cluster galaxies (without the contribution of background galaxies) inside $0.5\,R_{200}$. The value of K can be obtained from the best-fitting simulated cluster, without the addition of background galaxies. Without the restrictive imposition of homogeneity of the LF, which is quite surely *not* valid in general, we will measure different LFs for different control areas. The 'real' cluster LF will be obtained only in the limit situation where not a single cluster galaxy is found inside the control area. This will probably not happen with our sample: our limited imaging field of view is not much larger than the virial radius of the cluster, so even if we define control areas as distant from the centre as our image allows, the small background would not render a statistically significant sample. We have then used as control area the region beyond $1.2\,R_{200}$, which contains a large enough sample of background galaxies and is as far away from the cluster centre as the image allows. In the best-fitting simulated distribution, only 16 galaxies (around 8 per cent) of the total cluster galaxies are situated in this region. If these galaxies are not representative of the central $0.5\,R_{200}$, equation (10) will not hold, and the number counts in each magnitude bin will be affected, so we have added in quadrature to the standard errors of $N(m)$ twice the estimated (Poisson) errors in each magnitude bin due to these galaxies. This will not prevent systematic errors, but will give more realistic estimates of the errors in each bin and in the estimated LF parameters. Fig. 13 shows the resulting cluster LF. Superimposed to each LF, we have plotted the best-fitting Schechter law (Schechter 1976):

$$\phi(m) = 0.4\ln(10)\,\phi^*\,10^{0.4(\alpha+1)(m^*-m)}\,{\rm e}^{-10^{0.4(m^*-m)}}. \qquad (11)$$

We have obtained $\alpha = -1.16 \pm 0.18$ and $m^\star = 22.36 \pm 0.30$. The characteristic magnitude was converted to absolute M_i magnitudes using a global *K*-correction calculated with a spectral energy distribution of a typical elliptical galaxy at the cluster redshift; we have obtained $M^\star = -21.44 \pm 0.30$. The obtained LF for LCDCS-S001 is only slightly steeper than a flat LF. This agrees with typical values of α for rich clusters at low- and intermediate-redshift clusters (Mobasher et al. 2003; Rines & Geller 2008). However, we must

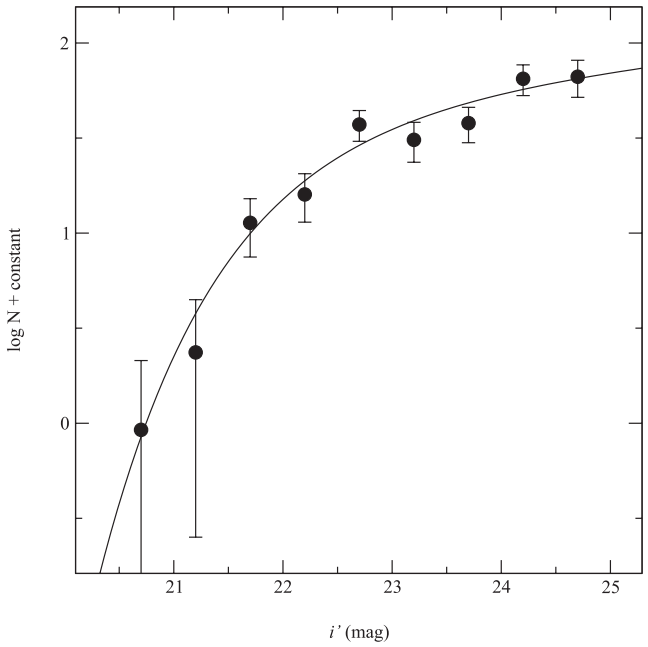

Figure 13. LF of the cluster in the i' band, and best-fitting Schechter function.

interpret this result with caution once this reflects mainly the most central galaxies in our sample and our photometry does not extend to faint magnitudes (we cannot exclude, say, an upturn for fainter magnitudes, like the one found by, e.g., De Propris et al. 1995). Our characteristic magnitude agrees very well with the results of Rudnick et al. (2009); note, however, that these authors have found a lowering of the cluster faint-end at $0.6 < z < 0.8$, which could be attributed, e.g., to the destruction of low-mass galaxies in the cluster environment; this was not observed in LCDCS-S001.

8 CONCLUSIONS

We present new spectroscopic measurements and the photometric parameters of the galaxies in the direction of the galaxy cluster LCDCS-S001. i' and r' imaging was obtained and the individual sources were extracted. For the individual sources, we have derived magnitudes, relative positions and the bulge+disc decomposition of their light profiles. This allowed us to analyse the projected distribution of galaxies, to derive structural parameters of the individual galaxies and to improve previous estimates of the kinematic parameters. Our main results can be summarized as follows.

(i) LCDCS-S001 has a velocity dispersion of $\sigma = 887 \pm 249\,\mathrm{km\,s^{-1}}$, a virial radius $R_{200} = 0.98 \pm 0.22\,\mathrm{Mpc}$ and a mass of $M_{200} = (5.4 \pm 2.8) \times 10^{14}\,\mathrm{M}_{\odot}$.

(ii) The cluster has an elongated morphology in the north–south direction with $\varepsilon = 0.49 \pm 0.14$, being well represented by a King model with $R_{\mathrm{C}} = 283 \pm 66\,\mathrm{kpc}$, above the typical core radii of regular clusters.

(iii) Besides showing a flat morphology, LCDCS-S001 presents indications of peripheral substructures, in particular a very compact one at north-west from the cluster centre. This local overdensity, albeit not comprehending a large number of galaxies, reaches densities comparable to the cluster centre and is inhabited by one confirmed cluster member.

(iv) LCDCS-S001 presents an i' LF with $\alpha = -1.16 \pm 0.18$, compatible with a flat faint-end, typical of rich clusters both in low and high redshifts.

(v) A large fraction (∼50–70 per cent, depending on the B/T boundary) of the cluster members have B/T values compatible with late-type galaxies. This high proportion of late-type galaxies is compatible with other rich clusters at similar redshift and shows that evolutionary effects change dramatically the morphological mix of clusters of galaxies at least from $z \sim 0.7$ to the present.

The data above show that LCDCS-S001 is a moderately rich cluster of galaxies, with a large core and flat morphology, presenting a pronounced central concentration and at least one important projected substructure, and rich in late-type galaxies. All these, together with the analyses presented in Paper I, reinforce the view that this cluster is still in process of collapse and capture of peripheral material. Whatever the physical processes which drive the morphological evolution of galaxies in clusters, they will reduce the late-type galaxy fraction in some time-scale, while producing little evolution of the LF, what can indicate that the creation and destruction of lower luminosity galaxies tend to compensate each other, at least during part of the evolution of clusters of galaxies.

ACKNOWLEDGMENTS

The authors are grateful to C. Bonatto for useful discussions and acknowledge the financial support of the Brazilian institution CNPq. We also thank two anonymous referees for greatly helping us to improve our statistical analyses.

This work is based on observations obtained at the Gemini Observatory, which is operated by the Association of Universities for Research in Astronomy, Inc., under a cooperative agreement with the NSF on behalf of the Gemini partnership: the National Science Foundation (USA), the Science and Technology Facilities Council (UK), the National Research Council (Canada), CONICYT (Chile), the Australian Research Council (Australia), Ministério da Ciência e Tecnologia (Brazil) and Ministerio de Ciencia, Tecnología e Innovación Productiva (Argentina).

REFERENCES

Beers T. C., Flynn K., Gebhardt K., 1990, AJ, 100, 32
Berrier J. C., Stewart K. R., Bullock J. S., Purcell C. W., Barton E. J., Wechsler R. H., 2009, ApJ, 690, 1292
Bertin E., Arnouts S., 1996, A&AS, 117, 393
Biernacka M., Flin P., Panko E., 2009, ApJ, 696, 1689
Boschin W., Barrena R., Girardi M., 2009, A&A, 495, 15
Bravo-Alfaro H., Caretta C. A., Lobo C., Durret F., Scott T., 2009, A&A, 495, 2
Burgett W. S., Vick M. M., Davis D. S., Colless M., De Propris R., 2004, MNRAS, 352, 605
Carter D., Metcalfe N., 1980, MNRAS, 191, 325
Chen H. W. et al., 2002, ApJ, 570, 54
Cheng J. Y., Faber S. M., Simard L., Graves G. J., Lopez E. D., Yan R., Cooper M. C., 2011, MNRAS, 412, 727
De Propris R., Pritchet C. J., Harris W. E., McClure R. D., 1995, ApJ, 450, 534
de Theije P. A. M., Katgert P., van Kampen E., MNRAS, 273, 30
Demarco R. et al., 2007, ApJ, 663, 164
Fasano G., Poggianti B. M., Couch W. J., Bettoni D., Kjaergaard P., Moles M., 2000, ApJ, 542, 673
Finn R. A. et al., 2005, ApJ, 630, 206
Girardi M., Biviano A., Giuricin G., Mardirossian F., Mezzetti M., 1995, ApJ, 438, 527

Girardi M., Giuricin G., Mardirossian F., Mezzetti M., Boschin W., 1998, ApJ, 505, 74
Häussler B. et al., 2007, ApJS, 172, 615
Hopkins P. F., Bahcall N. A., Bode P., 2005, ApJ, 618, 1
Hoyos C. et al., 2011, MNRAS, 411, 2439
Hwang H. S., Lee M. G., 2009, MNRAS, 397, 2111
Just D. W., Zaritsky D., Sand D. J., Desai V., Rudnick G., 2010, ApJ, 711, 192
Kodama T., Smail I., Nakata F., Okamura S., Bower R. G., 2001, ApJ, 562, L9
Krabbe A. C., Rembold S. B., Pastoriza M. G., 2007, MNRAS, 378, 569
Lewis I. et al., 2002, MNRAS, 334, 673
Lubin L. M., Postman M., Oke J. B., Ratnatunga K. U., Gunn J. E., Hoessel J. G., 1998, AJ, 116, 584
Lubin L. M., Oke J. B., Postman M., 2002, AJ, 124, 1905
McGee S. L., Balogh M. L., Bower R. G., Font A. S., McCarthy I. G., 2009, MNRAS, 400, 937
Mobasher B. et al., 2003, ApJ, 587, 605
Moran S. M., Loh B. L., Ellis R. S., Treu T., Bundy K., MacArthur L. A., 2007, ApJ, 665, 1067
Panko E., Juszczyk T., Biernacka M., Flin P., 2009, ApJ, 700, 1686
Park C., Hwang H. S., 2009, ApJ, 699, 1595
Peng C. Y., Ho L. C., Impey C. D., Rix H.-W., 2002, AJ, 124, 266
Plionis M., 2002, ApJ, 572, L67
Plionis M., Tovmassian H. M., Andernach H., 2009, MNRAS, 395, 2
Poggianti B. M. et al., 2009, ApJ, 697, L137
Rafelski M., Wolfe A. M., Cooke J., Chen H. W., Armandroff T. E., Wirth G. D., 2009, ApJ, 703, 2033
Rahman N., Krywult J., Motl P. M., Flin P., Shandarin S. F., 2006, MNRAS, 367, 838
Rembold S. B., Pastoriza M. G., 2007, MNRAS, 374, 1056 (Paper I)
Rhee G. F. R. N., van Haarlem M. P., Katgert P., 1989, A&AS, 91, 513
Rines K., Geller M. J., 2008, AJ, 135, 1837
Rudnick G. et al., 2009, ApJ, 700, 1559
Schechter P., 1976, ApJ, 203, 297
Shim H., Im M., Pak S., Choi P., Fadda D., Helou G., Storrie-Lombardi L., 2006, ApJS, 164, 435
Simard L., 1998, in Albrecht R., Hook R. N., Bushouse H. A., eds, ASP Conf. Ser. Vol. 145, Astronomical Data Analysis Software and Systems VII. Astron. Soc. Pac., San Francisco, p. 108
Simard L. et al., 2009, A&A, 508, 1141
Strazzullo V., Paolillo M., Longo G., Puddu E., Djorgovski S. G, De Carvalho R. R., 2005, MNRAS, 359, 191
Struble M. F., Ftaclas C., 1994, AJ, 108, 1
Tanaka M., Kodama T., Arimoto N., Tanaka I., 2005, MNRAS, 365, 1392
Tran K.-V. H., Simard L., Zabludoff A. I., Mulchaey J. S., 2001, ApJ, 549, 172
van Dokkum P. G., Franx M., Fabricant D., Illingworth G. D., Kelson D. D., 2000, ApJ, 541, 95
West M. J., Dekel A., Oemler A., Jr, 1989, ApJ, 336, 46

This paper has been typeset from a TEX/LATEX file prepared by the author.